

Simultaneous optical and multi-band terahertz imaging using an atomic quantum sensor.

ANDREW RAE MACKELLAR^{*1}, C. STUART ADAMS¹, AND KEVIN J. WEATHERILL¹

¹Quantum Light and Matter Group, Department of Physics, Durham University, South Road, Durham DH1 3LE, United Kingdom

^{*}andrew.r.mackellar@durham.ac.uk

Compiled December 2, 2025

We demonstrate simultaneous imaging at 0.549 THz and 1.012 THz with an optical overlay using a two-species atomic-vapour-based technique. The atomic vapour, comprising laser-pumped rubidium and caesium atoms contained within the same cell, is used to convert two narrowband terahertz signals to optical frequencies which can then be detected using standard CMOS sensors. We use the system to image and perform spectral analysis of material samples. As atomic vapour is optically transparent, by using optically-transparent terahertz lenses, we can achieve simultaneous optical imaging, allowing for potential integration of terahertz sensitivity into a range of optical imaging devices.

<http://dx.doi.org/10.1364/ao.XX.XXXXXX>

1. INTRODUCTION

Hyperspectral and multispectral imaging techniques enable simultaneous acquisition of spatial and spectral information, allowing for the identification and classification of materials based on their spectral signatures. These techniques are widely employed in applications such as food quality assessment [1–3], environmental monitoring [4, 5], security inspection [6], and biomedical imaging [7–10]. Conventional multispectral systems typically operate in the visible and near-infrared (VIS–NIR) spectral regions, where material discrimination is achieved by leveraging reflectance differences across discrete wavelength bands [11–13].

Terahertz (THz) imaging, covering the spectral range from approximately 0.3 to 3 THz, offers complementary capabilities to VIS–NIR modalities. Owing to the non-ionizing nature of THz radiation and its ability to penetrate many non-metallic, non-polar materials [14, 15], THz imaging enables non-destructive probing of subsurface structures [16, 17]. Furthermore, numerous materials exhibit distinct spectral features in the THz range due to molecular vibrational and rotational resonances, providing a basis for chemical identification [18–20]. These properties have led to increasing interest in THz multispectral and hyperspectral imaging for applications in agriculture [21, 22], cultural heritage diagnostics [23–26], medical imaging (e.g., cancer margin detection) [27–29], and the identification of concealed substances and illicit materials [30, 31].

Several imaging modalities have been developed for the THz domain, each optimized for specific application requirements. Time-domain spectroscopy (THz-TDS) is commonly employed when high spectral resolution and broadband coverage are needed [32–34]. However, TDS-based imaging typically re-

quires raster scanning, resulting in slow acquisition times for two-dimensional images.

In contrast, focal plane array (FPA) detectors, such as microbolometer and field-effect transistor (FET) arrays, enable rapid acquisition of two-dimensional images in a single exposure [35]. While advantageous for high-throughput imaging, these systems generally lack intrinsic spectral resolution and may exhibit limitations in sensitivity and temporal response.

Hybrid imaging architectures have emerged to address the trade-offs between spectral fidelity and acquisition speed. Such systems combine FPAs with tuneable THz sources or discrete-frequency THz emitters to enable multispectral imaging with improved temporal performance [36]. These approaches offer a promising route toward practical, real-time THz imaging systems capable of balancing spectral and spatial resolution with acquisition throughput. However, the speed and sensitivity of the THz camera remains the limitation in these systems.

Recently, new approaches to terahertz sensing have emerged using atom-based quantum sensors [37]. Atomic THz sensors generally operate by mapping incoming THz signals on to infrared or optical fields. Previous work has demonstrated high-speed full-field imaging at kilohertz frame rates [38–40] and has enabled a range of optical techniques to be transferred to the THz range, such as super-resolution imaging [41] and fast readout of orbital angular momentum beams [42].

Because these atom-based sensors use narrowband atomic transitions that are well described by theory [43], they are intrinsically calibrated and can provide electric-field measurements that are linked to SI-units [44, 45]. However, due to the discrete resonant frequency of the atomic transition they are limited to operation at particular discrete frequencies and, although rapid

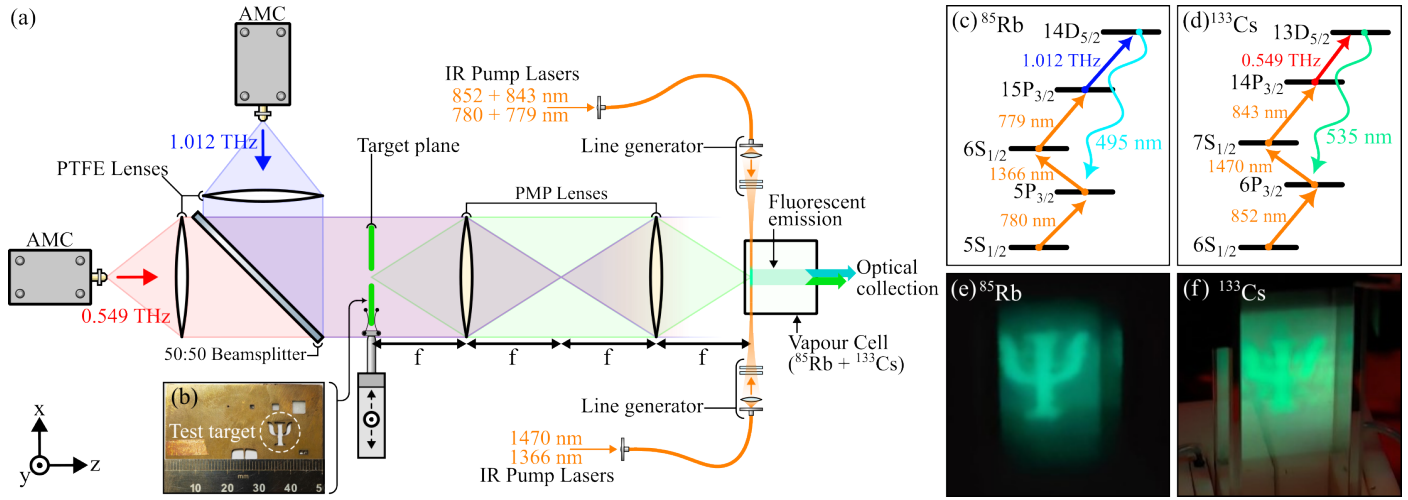


Fig. 1. Experimental setup of the two-species imager (a). Two fields at 0.549 THz (red) and 1.012 THz (blue) are collimated with $f=75$ mm lenses, and then overlapped by a high resistivity float zone (HRFZ) Si beamsplitter such that the beams are co-linear. This combined bi-chromatic field interacts with a target object, and is then re-imaged by a polymethylpentene (PMP) lens relay such that light from the target plane is refocused into the science cell at the position of a light sheet (orange). This light sheet excites the ^{85}Rb & ^{133}Cs atoms to states with transitions that are resonant with the 1.012 THz & 0.549 THz fields. In the presence of these fields, the atoms fluorescence at 495 nm (c) and 535 nm (d), respectively. Real-colour images of the optical fluorescence when imaging a ‘Y’ pattern from a metal test card (b) are shown in ^{85}Rb (e) and ^{133}Cs (f).

switching between frequencies is possible [46], up until now, only a single frequency at a time has been demonstrated. Here, we expand upon the operation of an atomic-vapour-based THz sensors: firstly; by using vapour comprised of two different atomic species, we can operate at two different THz frequencies simultaneously. Secondly, since the atomic vapour is transparent to optical frequencies, by using optically transparent THz lenses, we can also achieve a simultaneous optical overlay. We use the system to perform proof-of-principle materials analysis by differentiating between samples of different sugars.

2. EXPERIMENTAL SETUP

The experimental setup is shown in Figure 1a. Terahertz fields are emitted by Virginia Diodes Amplifier Multiplier Chains (VDI AMC331 & AMC731), supplied with radio frequencies generated by a Windfreak Technologies SynthHD PRO (v2) dual channel RF signal generator. One RF channel supplies 10, 159.54 MHz at 10 dBm to the AMC331 ($\times 54$ frequency multiplication) to output approximately 15 μW at 0.549 THz, with the field emission from a VDI WR1.5H (25) horn. The second channel supplies 10 dBm at 14,059.13 MHz to the AMC731 ($\times 72$ frequency multiplication) to generate approximately 190 μW at 1.012 THz, emitted via a VDI WR1.0DH horn. Both fields have a 10° full-width 3 dB divergence angle, and are vertically polarised. The terahertz fields are collimated with $f=75$ mm PTFE (Polytetrafluoroethylene) lenses, then overlapped with a HRFZ (High-Resistivity Float-Zone) silicon beam-splitter with a transmission:reflection ratio of approximately 55:45, generating a combined field that is projected along a main imaging axis (Figure 1, Z-axis).

This combined, bi-chromatic field illuminates a target object (Figure 1b), located at one focus of a 4-f imaging relay comprised of two $f=65$ mm polymethylpentene (PMP) lenses (Thorlabs AL265, polished to enable optical imaging), which refocus the THz fields into a vapour cell filled with atomic rubidium (natural abundance) and atomic caesium-133, configured to a magnification ratio of approximately 1:1, resulting in an effective

field of view of 1 cm^2 . This target object is mounted on a motorised (Figure 1, X-Y) translation stage to expand the accessible field of view beyond the limits of the vapour cell by rastering the target position within the imaging field plane. The vapour cell is constructed with a quartz glass Hellma fluorescence cuvette (Part no. 101-10-40), with an internal path length of 10×10 mm, filled and sealed under vacuum ($\approx 10^{-7}$ mbar). To generate approximately equal partial vapour pressures of each atomic vapour at typical experimental cell temperatures ($\approx 60^\circ\text{C}$), the cell has been filled with a ratio of approximately 2:1 Rb:Cs metal (by mass), accordingly with Raoult’s law [47].

To prepare the atoms in the vapour in THz-sensitive states we use a total of six excitation lasers. The excitation laser beams within the vapour cell are shaped by a pair of fibre-coupled light-sheet generators, comprised of a bare single-mode fibre-end followed by three cylindrical lenses. The first lens sets the working distance of the generator and the horizontal thickness of the light sheet, while the remaining two lenses first expand and then collimate the beam’s vertical aspect. These lenses are configured such that they create a thin sheet of light within the cell of approximately 15 mm height (y) and approximately $80\text{ }\mu\text{m}$ thickness (z), while the width of 10 mm (x) is determined by the internal dimensions of the cuboidal science cell.

The line generators are used to deliver light at wavelengths (with typical post-fibre powers) of: 852 nm (16 mW), 1470 nm (27 mW), 843 nm (130 mW), 780 nm (15 mW), 1366 nm (14 mW), and 779 nm (77 mW). These wavelengths correspond to transitions within the atomic vapours; the ^{133}Cs is pumped along the excitation pathway $6S_{1/2} \rightarrow 6P_{3/2} \rightarrow 7S_{1/2} \rightarrow 14P_{3/2}$, and similarly the ^{85}Rb is pumped via $5S_{1/2} \rightarrow 5P_{3/2} \rightarrow 6S_{1/2} \rightarrow 15P_{3/2}$ (see Figure 1c,d). When the atoms within the cell move into the light sheet, they are thereby optically pumped into excited ‘Rydberg’ states that have resonant transitions to nearby states with frequencies 0.549 THz (in ^{133}Cs) and 1.012 THz (in ^{85}Rb) to match the incoming THz fields. When these atoms are simultaneously exposed to both the IR pump lasers and THz fields,

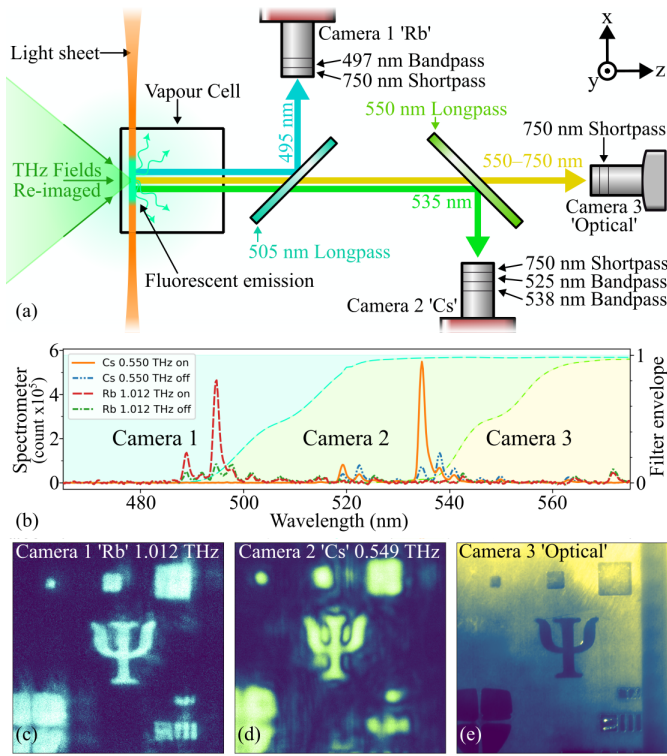


Fig. 2. A schematic of the spectral separation of the fluorescence emission from atomic vapour in the science cell (a). The excited ^{133}Cs and ^{85}Rb atoms fluoresce at 535 nm and 495 nm light in response to the presence of 0.549 THz and 1.012 THz fields, respectively. Dichroic mirrors (dash cyan & green lines) are used to direct wavelength-bands (coloured regions) containing the Rb and Cs fluorescence peaks towards cameras 1 & 2, while the remaining optical light is captured by camera 3 (b). These wavelength bands are filtered further with narrow-band filters, with the resulting data captured by each camera and processed is shown in (c–e).

they are further transferred into the $13\text{D}_{5/2}$ (^{133}Cs) and $14\text{D}_{5/2}$ (^{85}Rb) states, from where they decay via strong optical transitions back to the $6\text{P}_{3/2}$ and $5\text{P}_{3/2}$ states, emitting light at 535 nm and 495 nm, respectively. This process leads to strong emission on narrow transition lines, therefore generating optical fluorescence in the vapour that is spatially correlated with the incoming terahertz fields (see Figure 1e,f).

The resulting emission spectra from both atomic species is shown in Figure 2b, where the spectra from both the lower excited states ('THz off') and upper excited states ('THz on') are shown, with the emission from the ^{133}Cs predominantly in the two spikes near 535 nm and from the ^{85}Rb predominantly in the two spikes near 495 nm. This fluorescent emission is filtered with dichroic mirrors (Figure 2a,b) such that the light is spectrally separated into wavelength bands — $\lambda_{\text{Rb}} < 500$ nm, $500 \text{ nm} < \lambda_{\text{Cs}} < 550$ nm, $\lambda_{\text{optical}} > 550$ nm, represented here by the cyan, green, and yellow arrows and regions — and directed into optical cameras, with the 495 nm cyan light being reflected into the 'rubidium' camera (Thorlabs CC215MU cooled sCMOS), the 535 nm green light reflected into the 'caesium' camera (Thorlabs CC215MU cooled sCMOS), and the remaining optical yellow region showing light that enters the 'optical' camera (Thorlabs CS165MU CMOS). In this way spatial separation

is induced between the fluorescent response to the THz field at 0.549 THz, fluorescence induced by the 1.012 THz field, and optical scatter from the target sample, for isolated capture.

Each imaging arm then contains additional narrowband filters to isolate THz-induced fluorescent light from background fluorescence, scatter from IR pump lasers, and atomic decay emissions longer than 750 nm.

The resulting filtered images are shown in Figure 2c–e, for rubidium at 495 nm, for caesium at 535 nm, and the optical pass-through >550 nm. These are images of the test card shown in Figure 1b, swept by the motorised translation stage to expand the field-of-view beyond the constraints of the 10 mm-wide vapour cell, with sub-images stitched together (see Supplementary Document Section 2 for details on this processing).

3. IMAGE PROCESSING FOR MATERIALS ANALYSIS

To highlight the benefit of simultaneous multispectral imaging, we use the system to perform materials analysis of sugar samples. The samples used here are comprised of 11 mm diameter copper discs filled with the sugars glucose, maltose, lactose, ground and compressed into pellets. For comparison a similar sample of 100 % PTFE was also included. These samples were mounted in a 3d-printed polylactic acid (PLA) mount, affixed to a X-Y motorised translation stage for automated remote-control during the acquisition process.

To enable an extended field of view, images were captured piecewise by moving the target samples within the imaging plane (X-Y), each with an exposure of 100 ms. To allow for image processing, each camera captured two images at each target position: one image with the THz fields active, and a second image with the fields inactive ('THz_{on}' and 'THz_{off}' for each field state, respectively), while a third camera captures an optical image of the sample. Additionally, a single pair of 'brightfield' images (again with the THz fields active and inactive, 'Brightfield THz_{on}' and 'Brightfield THz_{off}') were captured with the target sample moved out of the field of view to capture variation in the THz field illumination without obstruction. These images were combined by way of the following algorithm:

$$\text{Image}_{\text{output}} = \frac{\left(\frac{\text{THz}_{\text{on}}}{\text{THz}_{\text{off}}} - 1 \right)}{\left(\frac{\text{Brightfield THz}_{\text{on}}}{\text{Brightfield THz}_{\text{off}}} - 1 \right)}, \quad (1)$$

...where the division of the THz_{on} image by the THz_{off} image compensates for variation in the light-sheet intensity both spatially over the field of view, and temporally with drifts in the pump laser power. Similarly, the denominator compensates for uneven THz field illumination in the object imaging plane. Examples of the resulting processed images can be seen in Figure 3a,b. Here we see a clear discrimination in the ratios of transmission at the two THz frequencies between the various samples; glucose, maltose, and lactose are easily distinguished.

To highlight the spectral difference between the two images we generate a vector map using the individual Cs and Rb fluorescence fields (Figure 3a,b) as the X and Y co-ordinates of a vector for each pixel pair in the sampled images. Wherever the pixel values in both Cs and Rb fields are similar, this generates vectors that lie along the diagonal of this vector space. Pixels that are different between the Cs and Rb fields instead generate vectors that lie in off-diagonal positions (Figure 3c). If we represent these vectors with a magnitude $|\mathbf{R}|$ and a phase angle ϕ , we can colour-code an output map to highlight spectral discrimination between the input Cs and Rb fields. We use a

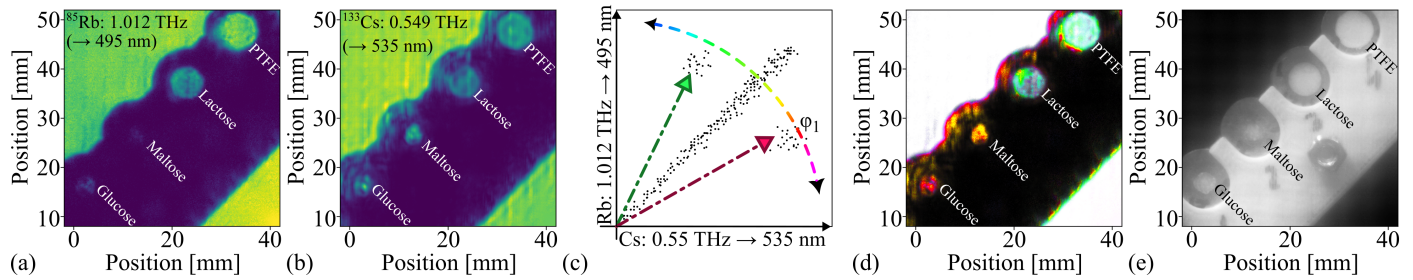


Fig. 3. Individual THz fields at 0.549 THz (a) and 1.012 THz (b), are used as X and Y co-ordinates, respectively, in a vector space (c). For each pixel pair, the resulting vector phase and magnitude is mapped to an HSL colour map. The resulting phasemap coloured by pixel phase (d), with the corresponding optical image is shown in (e).

Hue-Saturation-Lightness (HSL) colour-space mapping:

$$\begin{aligned} H &= \text{sign}(\phi - \phi_0) \times |\phi - \phi_0|^\alpha \times A, \\ S &= |\phi - \phi_0| \times B, \\ L &= |R|, \end{aligned} \quad (2)$$

...where α and A act as gain and gamma scaling of the the colour-wheel arc mapped to differences between transmission of the two THz fields, B acts as a gain control for the colourmap saturation to limit colour to image areas with a difference in transmission, and ϕ_0 an offset on the colour-wheel. These parameters have been tuned (with $A = 1.65$, $\alpha = 0.5$, $B = 7$, $\phi_0 = 0.15$) to highlight the differences between the input samples at the imaging frequencies of 0.549 THz and 1.012 THz. Spectral analysis of these samples shows that at 0.549 THz glucose has the highest absorption, while maltose and lactose have similar but slightly lower absorption than glucose; and at 1.012 THz the absorption of glucose rises significantly, maltose has an even greater increase in absorption than glucose, while lactose shows a significantly lower increase in absorption (Supplemental Document Section 1 contains broadband terahertz spectra of these sugar samples recorded using a Toptica Terascan photomixer system). The resulting coloured phasemap is shown in Figure 3d.

Image processing was performed on a laboratory computer with the Python Libraries Numpy [48], Scipy [49], and Pillow [50]. With modest computation power the data processing shown in Figure 3 was performed in 62 s. Of this, by far the largest processing cost was in stitching individual raster-scanned images into a single $42 \text{ mm} \times 42 \text{ mm}$ ‘widefield’ image for each of the two THz fields. Remaining processing required approximately 200 ms. When processing non-rastered data with a field-of-view limited by the vapour cell size (in this case $10 \text{ mm} \times 10 \text{ mm}$), this processing time falls to 34 ms, would could be further reduced to 12 ms with the use of hardware binning and cropping performed on-camera during capture. In this raster-less configuration the field of view could still be extended with the construction of a larger vapour cell [51].

Simultaneous to this entire process is the ‘optical’ field, to which only the widefield stitching algorithm has been applied in the data shown in Figure 3e. The atomic vapour is only non-transparent at wavelengths where an atomic transition is possible. This reduces the absorbed wavelengths to (1) the transitions which exist within the atom, and (2) to those which are

adjacent to an atomic state that is populated. As a result, the atomic vapour remains largely optically transparent, and the optical camera captures light determined by the dichroic mirrors used to separate the atomic fluorescence. This does result in ‘background’ atomic fluorescence from the lower excited $14P_{3/2}$ (Cs) and $15P_{3/2}$ (Rb) states leaking into the optical images. This could be compensated for by pulsing the optical target illumination during the ‘THz off’ state, such that two optical images can be compared to perform common-mode rejection of background fluorescence as has been applied to the THz fluorescence in this work. Alternatively, the IR pump lasers used to excite the atomic vapour could be pulsed to deactivate fluorescence entirely during optical field capture, at the cost of adding a third ‘state’ to the duty cycle of image capture (in addition to ‘THz field on’ and ‘THz field off’).

4. CONCLUSION AND OUTLOOK

We have demonstrated simultaneous multispectral terahertz imaging using a two-atomic-species quantum sensor. The technique allows for rapid non-destructive materials analysis by comparing multiple two-point spectra in a 2D focal-plane-array format. Furthermore, we demonstrated the ability to simultaneously collect optical overlay images in the same optical pathway used by the THz imaging, due to the optically-transparent nature of the ‘atomic-sensor’. This could enable the addition of THz imaging to a range of optical instruments, potentially leading to the construction of new hybrid quantum sensors.

5. ACKNOWLEDGEMENTS

We thank Paul Dean, Alex Valavanis, Sanchit Kondawar, Andrew Burnett and Thomas Gill of the Electronics Engineering Department of Leeds University for stimulating discussions and for preparing the sugar samples analysed in this work. We thank Cyril Bourgenot and Paul White of the Centre for Applied Instrumentation and Lee Bainbridge of the Physics Department at Durham University for aid in polishing the THz imaging lenses used in this work. We thank Malcolm Richardson of the Chemistry Department of Durham University for aid in the construction and filling of the vapour cells used in this work. We acknowledge funding from the UK Engineering and Physical Sciences Research Council grants EP/W033054/1 and EP/Z533166/1.

REFERENCES

1. A. A. Gowen, C. P. O'Donnell, P. J. Cullen, *et al.*, "Hyperspectral imaging—an emerging process analytical tool for food quality and safety control," *Trends Food Sci. & Technol.* **18**, 590–598 (2007).
2. D. Udayanga, A. Serasinghe, S. Dassanayake, *et al.*, "Dual-mode multispectral imaging system for food and agricultural product quality estimation," *IEEE Trans. on Instrum. Meas.* **73**, 1–12 (2024).
3. K.-S. Lee, "Multispectral food classification and caloric estimation using convolutional neural networks," *Foods* **12** (2023).
4. S. Kvaterniuk, O. Kvaterniuk, V. Petruk, *et al.*, "Multispectral environmental monitoring of phytoplankton pigment parameters in aquatic environments," in *Photonics Applications in Astronomy, Communications, Industry, and High-Energy Physics Experiments 2019*, vol. 11176 R. S. Romaniuk and M. Linczuk, eds., International Society for Optics and Photonics (SPIE, 2019), p. 111762R.
5. T. Arnold, M. De Biasio, A. Fritz, and R. Leitner, "Uav-based multispectral environmental monitoring," in *SENSORS, 2010 IEEE*, (2010), pp. 995–998.
6. N. Vetrek, R. Ramachandra, S. Venkatesh, *et al.*, "Does complimentary information from multispectral imaging improve face presentation attack detection?" in *2024 IEEE Applied Sensing Conference (AP-SCON)*, (2024), pp. 1–4.
7. G. Lu and B. Fei, "Medical hyperspectral imaging: a review," *J. Biomed. Opt.* **19**, 010901 (2014).
8. E. V. Goessinger, P.-G. Dittich, P. Nöcker, *et al.*, "Classification of melanocytic lesions using direct illumination multispectral imaging," *Sci. Reports* **14**, 19036 (2024).
9. F. Ma, M. Yuan, and I. Kozak, "Multispectral imaging: Review of current applications," *Surv. Ophthalmol.* **68**, 889–904 (2023).
10. H. Ozkan, M. Aydin, O. A. Ozcan, and U. Zengin, "A portable multispectral vein imaging system," *J. Electr. Eng.* **74**, 64–69 (2023).
11. J. Van Beek, L. Tits, B. Somers, and P. Coppin, "Stem water potential monitoring in pear orchards through worldview-2 multispectral imagery," *Remote. Sens.* **5**, 6647–6666 (2013).
12. D. Stow, C. J. Nichol, T. Wade, *et al.*, "Illumination geometry and flying height influence surface reflectance and ndvi derived from multispectral uas imagery," *Drones* **3** (2019).
13. F. J. Burgos-Fernández, T. Alterini, F. Díaz-Doutón, *et al.*, "Reflectance evaluation of eye fundus structures with a visible and near-infrared multispectral camera," *Biomed. Opt. Express* **13**, 3504–3519 (2022).
14. S.-H. Wu, S. M. Latifi, C.-M. Mai, and S.-H. Yang, "A hybrid optical-electrical neural network for terahertz computational imaging," in *2024 49th International Conference on Infrared, Millimeter, and Terahertz Waves (IRMMW-THz)*, (2024), pp. 1–2.
15. Y. Ma, L. Shen, Y. Cao, *et al.*, "Aerogel defect detection using terahertz waves," in *2024 49th International Conference on Infrared, Millimeter, and Terahertz Waves (IRMMW-THz)*, (2024), pp. 1–2.
16. J. F. Federici, B. Schulkin, F. Huang, *et al.*, "Thz imaging and sensing for security applications—explosives, weapons and drugs," *Semicond. Sci. Technol.* **20**, S266 (2005).
17. H. Medjadba, H. Zehaf, and M. Lazoul, "Concealed objects detection and recognition in active transmission sub-terahertz imaging scanner for automatic security screening," *Opt. Eng.* **64**, 079801 (2025).
18. M. Tonouchi, "Cutting-edge terahertz technology," *Nat. Photonics* **1**, 97–105 (2007).
19. A. Bratu, M. Bojan, C. Popa, and M. Petrus, "Infrared to terahertz identification of chemical substances used for the production of ieds," *Spectrochimica Acta Part A: Mol. Biomol. Spectrosc.* **312**, 124055 (2024).
20. K. Singh, D. Garg, A. Bandyopadhyay, and A. Sengupta, "Dual spectroscopic detection of thz energy modes of critical chemical compounds," *Spectrochimica Acta Part A: Mol. Biomol. Spectrosc.* **271**, 120923 (2022).
21. M. Mathialagan and M. Esakkimuthu, "Study on applicability of terahertz imaging for microplastic identification in soil sample," *Opt. Eng.* **64**, 064107 (2025).
22. Q. Wang, A. C. Y. Goay, D. Mishra, and S. Atakaramians, "Convolutional neural network based terahertz imaging for detecting grass seed infestation," in *2024 49th International Conference on Infrared, Millimeter, and Terahertz Waves (IRMMW-THz)*, (2024), pp. 1–2.
23. E. Pickwell and V. P. Wallace, "Biomedical applications of terahertz technology," *J. Phys. D: Appl. Phys.* **39**, R301 (2006).
24. K. Bertling, J. Tornaiainen, A. Rakić, *et al.*, "Terahertz quantum cascade laser feedback imaging for cultural heritage preservation," in *2024 49th International Conference on Infrared, Millimeter, and Terahertz Waves (IRMMW-THz)*, (2024), pp. 1–2.
25. D. A. Vazquez, L. Pillozzi, E. DelRe, *et al.*, "Terahertz imaging super-resolution for documental heritage diagnostics," *IEEE Trans. on Terahertz Sci. Technol.* **14**, 455–465 (2024).
26. R. M. Groves, B. Pradarutti, E. Kouloumpi, *et al.*, "Multi-sensor evaluation of a wooden panel painting using terahertz imaging and shearography," in *O3A: Optics for Arts, Architecture, and Archaeology II*, vol. 7391 L. Pezzati and R. Salimbeni, eds., International Society for Optics and Photonics (SPIE, 2009), p. 73910E.
27. Z. Yan, L.-G. Zhu, K. Meng, *et al.*, "Thz medical imaging: from in vitro to in vivo," *Trends Biotechnol.* **40**, 816–830 (2022).
28. Z. D. Taylor, R. S. Singh, D. B. Bennett, *et al.*, "Thz medical imaging: in vivo hydration sensing," *IEEE Trans. on Terahertz Sci. Technol.* **1**, 201–219 (2011).
29. S. Sung, N. Bajwa, N. Fokwa, *et al.*, "Fast-scanning THz medical imaging system for clinical application," in *Terahertz Emitters, Receivers, and Applications III*, vol. 8496 M. Razeghi, A. N. Baranov, H. O. Everitt, *et al.*, eds., International Society for Optics and Photonics (SPIE, 2012), p. 84960S.
30. W. L. Chan, J. Deibel, and D. M. Mittleman, "Thz spectroscopy and imaging for defense and security applications," *Reports on Prog. Phys.* **70**, 1325 (2007).
31. K. Kawase, Y. Ogawa, Y. Watanabe, and H. Inoue, "Non-destructive terahertz imaging of illicit drugs using spectral fingerprints," *Opt. Express* **11**, 2549–2554 (2003).
32. P. U. Jepsen, D. G. Cooke, and M. Koch, "Terahertz spectroscopy and imaging—modern techniques and applications," *Laser & Photonics Rev.* **5**, 124–166 (2011).
33. S. Eliet, A. Cuisset, F. Hindle, *et al.*, "Broadband super-resolution terahertz time-domain spectroscopy applied to gas analysis," *IEEE Trans. on Terahertz Sci. Technol.* **12**, 75–80 (2022).
34. N. A. Nikolaev, A. A. Rybak, and S. A. Kuznetsov, "Application of metasurface-based low-pass filters for improving thz-tds characteristics," *J. Physics: Conf. Ser.* **1461**, 012118 (2020).
35. S. Kojima, M. Suzuki, T. Okada, and K. Kawase, "Real-time terahertz imaging using a 320×240 microbolometer focal-plane array," *Opt. Express* **25**, 8511–8519 (2017).
36. W. L. Chan, G. M. Rebeiz, and D. M. Mittleman, "A review of passive millimeter-wave imaging technology," *IEEE Trans. on Microw. Theory Tech.* **62**, 2787–2800 (2014).
37. C. G. Wade, N. Šibalić, N. R. de Melo, *et al.*, "Real-time near-field terahertz imaging with atomic optical fluorescence," *Nat. Photonics* **11**, 40 (2017).
38. L. A. Downes, A. R. MacKellar, D. J. Whiting, *et al.*, "Full-field terahertz imaging at kilohertz frame rates using atomic vapor," *Phys. Rev. X* **10**, 011027 (2020).
39. L. A. Downes, L. Torralbo-Campo, and K. J. Weatherill, "A practical guide to terahertz imaging using thermal atomic vapour," *New J. Phys.* **25**, 035002 (2023).
40. X. Li, T. Li, J. Wan, *et al.*, "Dual-cameras terahertz imaging with multi-kilohertz frame rates and high sensitivity via rydberg-atom vapor," *J. Phys. D: Appl. Phys.* **58**, 085109 (2024).
41. J. P. Fleming, L. A. Downes, J. M. Girkin, and K. J. Weatherill, "Virtually structured illumination for terahertz super-resolution imaging," *Opt. Express* **33**, 26509–26516 (2025).
42. L. A. Downes, D. J. Whiting, C. S. Adams, and K. J. Weatherill, "Rapid readout of terahertz orbital angular momentum beams using atom-based imaging," *Opt. Lett.* **47**, 6001–6004 (2022).
43. N. Šibalić, J. D. Pritchard, C. S. Adams, and K. J. Weatherill, "Arc: An open-source library for calculating properties of alkali rydberg atoms," *Comp. Phys. Commun.* **220**, 319 (2017).

44. S. Chen, D. J. Reed, A. R. MacKellar, *et al.*, "Terahertz electrometry via infrared spectroscopy of atomic vapor," *Optica* **9**, 485–491 (2022).
45. W. Krokosz, J. Nowosielski, B. Kasza, *et al.*, "Electric-field metrology of a terahertz frequency comb using rydberg atoms," (2025).
46. L. A. Downes, C. S. Adams, and K. J. Weatherill, "Temporally-multiplexed dual-frequency terahertz imaging at kilohertz frame rates," *IEEE Trans. on Terahertz Sci. Technol.* pp. 1–5 (2025).
47. F. R. Foulkes, *Physical Chemistry for Engineering and Applied Sciences* (CRC Press, Milton, 2013), 1st ed.
48. C. R. Harris, K. J. Millman, S. J. van der Walt, *et al.*, "Array programming with NumPy," *Nature* **585**, 357–362 (2020).
49. P. Virtanen, R. Gommers, T. E. Oliphant, *et al.*, "SciPy 1.0: Fundamental Algorithms for Scientific Computing in Python," *Nat. Methods* **17**, 261–272 (2020).
50. A. Clark, "Pillow (pil fork) documentation," (2015).
51. B. Zhang, J. Wan, T. Li, *et al.*, "50 mm × 50 mm cesium atomic vapor cell for terahertz imaging: Implementation and application," (2025).